Materials and Solidification

Research Article

Lattice Boltzmann modeling of dendrite growth during ultrasonic-assisted solidification of an IN718 alloy

Zhentao Wang, Qingyu Zhang✉, Linkun Tan, Xiaonan Wang

Cite this article: Wang Z, Zhang Q, Tan L, et al. *Materials and Solidification* 2025, **1**(1): 9580002. https://doi.org/10.26599/MAS.2025.9580002

ABSTRACT: Dendrite growth during solidification of an IN718 alloy under forced convection induced by ultrasonication was simulated via the coupled cellular automaton–lattice Boltzmann (CA–LB) model. To demonstrate the validity of the LB modeling of ultrasonic propagation, the LB simulation results of acoustic attenuation in the melt are well compared with those of an analytical model reported in the literature. The CA–LB model was then used to simulate the growth of equiaxed and columnar dendrites under different ultrasonic amplitudes in the nonequilibrium solidification process. The simulation results revealed that the presence of ultrasound drastically influenced the solute concentration field in the liquid. The distribution of liquid concentrations accelerated the growth of dendrite arms near the sound source but repressed the growth of those far from the sound source. For multiple equiaxed dendrites, the average liquid concentration was relatively low at the initial stage without ultrasonication, whereas the average liquid concentration at the end stage was relatively high. Ultrasound accelerated the growth rate of a portion of the columnar dendrites near the sound source, which influenced their competitive growth mode and affected the final morphology. The present work not only reproduced the morphological evolution of different types of dendrites under ultrasound effects but also revealed the complex interactions among ultrasound-induced convections, the solute concentration field, and the kinetics of dendrite growth.

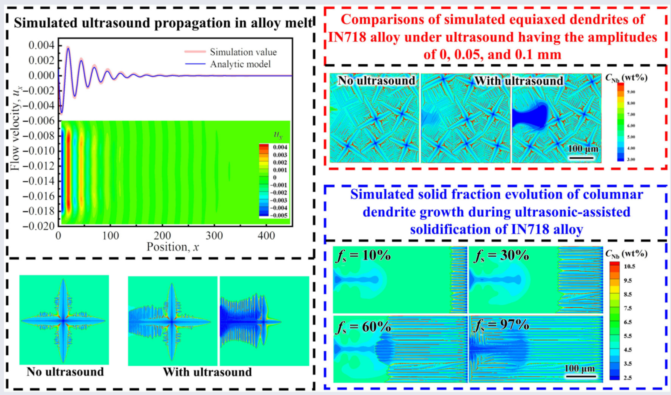

KEYWORDS: solidification dendrite; convection; numerical simulation; IN718 alloy; ultrasound

1 Introduction

Owing to the fact that an IN718 nickel-based superalloy has superior fatigue, radiation, and corrosion resistance, along with outstanding long-term structural stability, it is extensively employed in the production of high-temperature resistant parts in the fields of aero-engines and energy. Solidification during IN718 alloy processing (e.g., casting, welding, and additive manufacturing) is usually accompanied by melt convection, which can not only change the heat and mass transfer process in liquid but also play a key role in the formation of a solidification microstructure [1–4], thus affecting the performance of the final products.

In recent years, considerable attention has been given to the regulation of the microstructure and properties of IN718 alloys during solidification through experimental studies [5,6]. Nevertheless, observing the evolution of the solidification microstructure during experimental studies is challenging. The applications of numerical simulation can effectively incorporate aspects of the temperature field, dendrite growth velocity, and convective mass transfer so that the temperature field and velocity field evolution process during solidification can be observed in real-time with the aid of visualization [7,8]. Thus, numerical simulation studies of solidification microstructures have received persistent attention in both academia and engineering. Among various simulation approaches, cellular automaton (CA) and phase field (PF) are the most representative methods in terms of sharp interface and diffuse interface models, where the sharp interface model has higher computational efficiency [9,10]. Koepf *et al.* [11] conducted a three-dimensional CA simulation study on the growth orientation of columnar dendrites of the IN718 alloy during laser selective melting additive manufacturing. The laser spot size was regulated according to the simulation results. Xiao *et al.* [12] used the PF model to simulate the columnar dendrite growth process of the IN718 alloy under rapid solidification by laser additive manufacturing and explored the variation in the dendrite spacing and dendrite tip radius with

School of Iron and Steel, Soochow University, Suzhou 215137, China.

✉ Corresponding author. E-mail: qingyu.zhang@suda.edu.cn

Received: November 10, 2024; Revised: December 11, 2024; Accepted: January 17, 2025

different processing parameters. However, the above simulations did not consider the influence of microscale convection in the interdendritic liquid region on the concentration field in the mushy zone. Consequently, convection cannot be coupled with nonequilibrium solidification conditions, and the influence of convection on microstructure morphology and segregation has not yet been quantified.

The lattice Boltzmann (LB) model has developed quickly and is widely used for describing fluid flow and solute transport in the modeling of metallurgy and chemical reactions [13]. Owing to the microscopic nature of the LB models, it is feasible to handle any complex dendrite morphology at the solid–liquid boundaries. Therefore, in simulations of the solidification microstructure, the LB model has been well accepted for simulating fluid–solid coupling in the process of alloy solidification under convection [14,15]. Sun *et al.* [14] established a two-dimensional LB model [16–18] to simulate the growth of dendrites in binary alloys under the influence of forced convection. The transport phenomenon was described by the evolution of the moving particle distribution functions, and the fluid flow and solute transport controlled by convection and diffusion were solved in a highly efficient manner [18]. Following thorough analysis and validation of the model, it was subsequently used to simulate the growth of both single and multiple equiaxed dendrites in an Al–Cu alloy subjected to convective solidification conditions. Liu and Wang [19] established a multiscale physical model that simultaneously considers solute transport, phase transition, heat transfer, latent heat, and melt flow to simulate the microstructural evolution of alloys during nonequilibrium solidification. The PF method was employed in their research to simulate the dendritic growth of the alloy, and the heat transfer and fluid motion were simulated by the LB model. The intricate solidification microstructure in AM was predicted by their research.

Ultrasound has been widely used in modern solidification processing technology [20]. The role of an external ultrasonic field in metal solidification includes grain refinement, solute segregation reduction, and bubble elimination [21–26]. The ultrasonic waves cause strong convection in the melt, in which the evolution of the microstructure is significantly impacted. Hu *et al.* [27] investigated the impact of continuous and pulsed ultrasound on the microstructural evolution and mechanical property enhancement of a ternary $Cu_{68.3}Al_{27.6}Ni_{4.1}$ alloy. In their research, the size of the $\beta(Cu_3Al)$ phase was refined through different mechanisms under the influence of the two types of ultrasonication. A simultaneous increase in yield strength, superelastic deformation, and shape recovery was achieved due to the application of pulsed ultrasound. Li *et al.* [28] established a finite element numerical model and investigated the effects of varying ultrasonic power on the acoustic pressure field, temperature distribution, and flow dynamics during the solidification of 7085 aluminum alloy. On the basis of the results of numerical simulations, an ultrasonic power of 750 W was found to be most effective in enhancing the macroscopic physical fields, significantly increasing both the mass and heat transfer rates at the center of the melt. At present, research on the solidification microstructure of the IN718 alloy involves determining the dendritic morphology and segregation formation. However, few studies have investigated the impact of ultrasound-induced convection on the solidification of IN718 alloys.

In the present study, the morphological evolution of columnar and equiaxed dendrites during the ultrasonic-assisted solidification of an IN718 alloy was simulated after the validation of a coupled CA–LB model. The dendritic morphologies under the effect of an external ultrasonic field were reproduced, and quantitative data on the dendrite growth rate and solute field variation were obtained.

2 Materials and methods

2.1 Model description

The growth of equiaxed and columnar dendrites of an IN718 alloy under convective flow caused by ultrasonication was simulated. Within the computational domain, fluid flow and solute transport are described by the LB model, whereas nonequilibrium solidification is described by the CA model. The grid size was set to Δx = 1 μm. The domain size for the calculation of equiaxed dendrite growth was 500 μm × 500 μm, and the domain size for the calculation of columnar dendrite growth was 600 μm × 300 μm. When simulating the growth of a single equiaxed dendrite, the nucleus was placed in the center of the domain. When simulating the growth of multiple equiaxed dendrites, the nuclei were randomly placed. For the simulation of columnar dendrite growth, the nuclei were placed at the east wall of the domain, and the temperature gradient was imposed in the horizontal direction. Notably, the current work disregards the buoyancy effects caused by gravity. For simplicity, the IN718 alloy was regarded as a binary Ni–5 wt% Nb alloy [29,30]. The simulation parameters used in the present work are given in Table 1 [29]. The essence of the CA–LB model is described as follows.

Since the solidification phenomenon is driven by undercooling, in the CA model, the undercooling, ΔT, at the S/L interface is calculated as Eq. (1) [31]:

$$\Delta T = (T_m - m_l(V_n)C_l^*) - T^* - \Gamma K_w d(\theta) \tag{1}$$

where T_m is the melting point of pure nickel, V_n is the interface migration velocity, and m_l is the liquidus slope. C_l^* is the liquid concentration at the front of the S/L interface, and T^* is the actual interface temperature. Γ is the Gibbs–Thomson coefficient, and K_w is the curvature of the S/L interface. $d(\theta)$ is a function of surface anisotropy.

During the nonequilibrium solidification process, the interface migration velocity, V_n, for the IN718 alloy satisfies the following relationship (Eq. (2)) [32,33]:

$$V_n = a \cdot (\Delta T)^b \tag{2}$$

where a and b are the relevant kinetic coefficients. In accordance with the model proposed by Hunziker *et al.* [32], a = 1.2754×10^{-7} m/(s·$K^{3.05}$) and b = 3.05 were adopted in the present work.

According to the geometric feature of the CA cells, the relationship between the solid fraction increment and the interface velocity is given by Eq. (3):

Table 1 Simulation parameters used in present work [29]

Symbol	Definition and unit	Value
ρ	Density (kg/m³)	7620
T_m	Melting point of pure nickel (K)	1726.15
Γ	Gibbs–Thomson coefficient (K·m)	3.65×10^{-7}
K_p^{eq}	Equilibrium partition coefficient	0.48
m_l^{eq}	Equilibrium liquidus slope (K/wt%)	−10.5
D	Solute diffusion coefficient in solid (m²/s)	3×10^{-9}
μ	Dynamic viscosity of melt (Pa·s)	6.2×10^{-3}
ν	Kinematic viscosity of melt (m²/s)	8.1×10^{-7}

$$\Delta f_s = G_m \frac{v_n \Delta t}{\Delta x} \tag{3}$$

where Δf_s is the solid fraction increment, Δx is the cell size, Δt is the time step, and G_m is the geometric factor for reducing the mesh anisotropy.

The LB model was employed in this study to address fluid flow and solute transport. The governing equation of the LB model is given by Eq. (4) [33]:

$$f_i(x+c_i\Delta t, t+\Delta t) - f_i(x,t) = -\frac{1}{\tau}\left(f_i(x,t) - f_i^{eq}(x,t)\right)$$
$$i = 0,1,\cdots,8 \tag{4}$$

where $f_i(x,t)$ is the density distribution function of fluid particles and $f_i^{eq}(x,t)$ is the equilibrium distribution function. x, t, c_i, Δt, and τ are the position, time, discrete velocity, time step, and relaxation time, respectively.

The evolution of the solute distribution function, $g_i(x,t)$, with a source term can be written as Eq. (5) [14]:

$$g_i(x+c_i\Delta t, t+\Delta t) - g_i(x,t) = -\frac{1}{\tau_c}\left(g_i(x,t) - g_i^{eq}(x,t)\right) + G_i(x,t)$$
$$i = 0,1,\cdots,8 \tag{5}$$

where $g_i^{eq}(x,t)$ and τ_c are the equilibrium distribution function and relaxation time for solute transport, respectively. The amount of solute that is rejected into neighboring liquid cells as a result of solute partitioning during dendritic growth is represented by the source term $G_i(x,t)$.

The equilibrium distribution functions, $f_i^{eq}(x,t)$ and $g_i^{eq}(x,t)$ in Eqs. (4) and (5) can be written as Eqs. (6) and (7) [14]:

$$f_i^{eq}(x,t) = \omega_i \rho \left(1 + 3\frac{c_i \cdot u}{c^2} + \frac{9(c_i \cdot u)^2}{2c^4} - \frac{3u^2}{2c^2}\right) \tag{6}$$

$$g_i^{eq}(x,t) = \omega_i C \left(1 + 3\frac{c_i \cdot u}{c^2} + \frac{9(c_i \cdot u)^2}{2c^4} - \frac{3u^2}{2c^2}\right) \tag{7}$$

where ω_i is the weight coefficients ($\omega_0 = 4/9$, $\omega_{1-4} = 1/9$, and $\omega_{5-8} = 1/36$, respectively), ρ is the macroscopic density, which is calculated by $\rho = \sum_{i=0}^{8} f_i$. u is the velocity, which is calculated as $\rho u = \sum_{i=0}^{8} f_i c_i$. C is the composition, which is calculated by $C = \sum_{i=0}^{8} g_i$. c is the lattice speed, calculated by $c = \Delta x / \Delta t$. c_i represents the discrete velocities and can be written as Eq. (8) [14]:

$$c_i = \begin{bmatrix} 0, & c, & 0, & -c, & 0, & c, & -c, & -c, & c \\ 0, & 0, & c, & 0, & -c, & c, & c, & -c, & -c \end{bmatrix} \tag{8}$$

In our study, the ultrasound source was implemented through the regulation of the nonequilibrium extrapolation boundary conditions in the LB model. The flow velocity at the boundary caused by the ultrasound, u_{in}, can be written as Eq. (9):

$$u_{in} = A \sin(2\pi f t) \tag{9}$$

where A represents the ultrasound amplitude, and $f = 20{,}000$ is the frequency of the applied ultrasound.

2.2 Model validation

To demonstrate the validity of the ultrasound propagation calculation by using the LB model, the distribution of fluid velocity was computed and compared with the analytical solution in Ref. [34]. Given a sinusoidally varying velocity and density disturbance at the ultrasound source at the inlet, on the left boundary in this case, the analytical solution of the flow velocity distribution is shown in Eq. (10) [34]:

$$u_x(x,t) = A\exp(-a_s x)\sin\left(wt - \frac{2\pi}{\Lambda}x\right) \tag{10}$$

where $\mu_x(x,t)$ is the analytical solution of the flow velocity distribution, x is the distance from the left boundary, t is the time, a_s is the acoustic attenuation coefficient per unit length, w is the angular velocity, and Λ is the wavelength.

In addition to considering the viscosity of the medium, the two-dimensional acoustic attenuation coefficient also needs to be added to represent the influence of the wall. a_s in Eq. (6) is calculated by Ref. [34] (Eq. (11)):

$$a_s = \frac{4\pi^2 v}{c_s \Lambda^2} + \pi\left(\frac{8v\Lambda}{6\pi c_s L_y^2}\cos^2\left(\frac{1}{3}\arccos^{-1}\left(-\left(\frac{27v\Lambda}{16\pi c_s L_y^2}\right)^{\frac{1}{2}}\right)\right)\right)^{\frac{1}{2}} \tag{11}$$

where v is the kinematic viscosity, c_s is the speed of sound, and L_y is the length of the computation domain in the vertical direction.

In the LB simulation of ultrasonic propagation, the nonslip scheme was used on the wall of the computation domain. The velocity and density of the medium, as well as the perturbations, are given at the inlet, whereas the fully developed boundary conditions are used at the outlet. The transient velocity distribution in the liquid phase induced by the ultrasonic source at 100 cycles when $v = 0.2$ and $\Lambda = 25$ is displayed in Fig. 1. The inset displays the contour of the flow velocity. As illustrated in Fig. 1, the velocity distribution clearly oscillates, and the LB calculation is in good agreement with the analytical solution. The data overlay demonstrates the ability of the LB model to quantitatively describe ultrasound propagation within the melt.

3 Results and discussion

3.1 Simulation of single equiaxed dendrite growth

For single equiaxed dendrite growth, simulations were performed without ultrasonic waves and with ultrasonic waves with amplitudes of A = 0.05 and 0.1 mm. The cooling rate was set as CR = 500 K/s. As the solidification proceeded, the equiaxed dendrites started to grow, and the morphologies of the equiaxed dendrites with different solid phase fractions are shown in Fig. 2. CNb represents the mass fraction of solute Nb. Figures 2(a)–2(c)

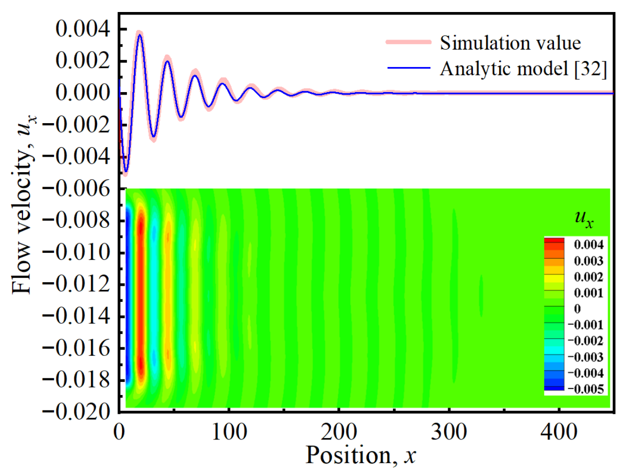

Fig. 1 Comparison of fluid velocity distributions calculated via LB model and analytical model.

清华大学出版社 Tsinghua University Press | SciOpen

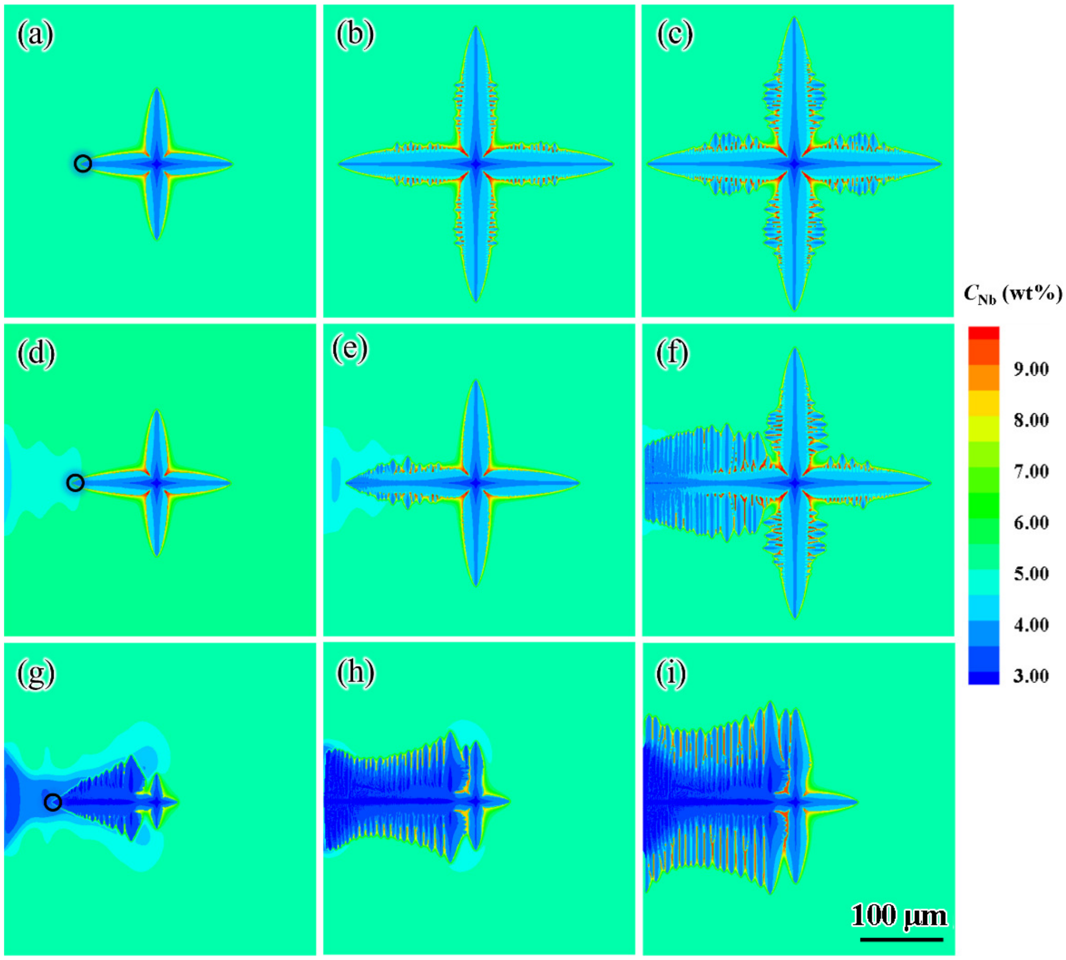

Fig. 2 Simulated morphological evolution of a single equiaxed dendrite shown by concentration of solute Nb under conditions (a–c) without ultrasound and (d–f) with ultrasound having amplitudes of A = 0.05 mm and (g–i) A = 0.1 mm. Solid fractions of insets are (a, d, g) f_s = 5%, (b, e, h) f_s = 15%, and (c, f, i) f_s = 25%, respectively.

present the dendrite morphology when there was no ultrasonic wave, with solid phase fractions of f_s = 5%, 15%, and 25%, respectively. Figures 2(d)–2(f) and 2(g)–2(i) show the equiaxed dendrites when the ultrasonic amplitude was A = 0.05 and 0.1 mm, respectively. In the absence of an ultrasonic source, the equiaxed dendrites exhibit symmetrical morphologies. After the addition of ultrasonic waves, the growth of the dendrite arm near the ultrasonic sound source was obviously faster than that of the other three arms, and it had more secondary dendrite arms. However, the growth of the dendrite arms in the opposite direction of the ultrasonic source obviously decreased, and the number of secondary dendrite arms was also lower than that of the other arms. As the ultrasonic amplitude increased, the growth velocity of the dendrite arm increased when it was close to the ultrasonic source.

Quantitative analysis of the length and growth rate of the dendrite arms located near the ultrasound source (left side), which are marked by black circles in Figs. 2(a), 2(d), and 2(g), respectively, was performed. Figure 3(a) shows the evolution of the dendritic arm length. When the ultrasonic wave was not added, the time for the dendrite tip to touch the boundary of the calculation domain was t = 0.101 s. When the ultrasonic wave was added with an ultrasonic amplitude of A = 0.05 mm, the time for the dendrite tip to contact the domain boundary was reduced to t = 0.095 s. As the ultrasonic amplitude was increased to A = 0.1 mm, the dendrite tip touched the boundary after t = 0.067 s. When the ultrasonic wave was introduced, the growth time before the dendrite tip contacted the boundary clearly decreased as the amplitude of the ultrasonic wave increased. Figure 3(b) shows a plot of the dendrite tip growth rate obtained by deriving the dendrite arm length over time. The peak velocities of dendrite tip growth are observed to be v_{max} = 10.45, 13.69, and 15.48 mm/s for the cases without ultrasound and with ultrasonic amplitudes of A = 0.05 and 0.1 mm. This shows that the peak velocity of dendrite tip growth without ultrasound was significantly lower than that in the cases with ultrasound. Moreover, the greater the amplitude of the applied ultrasonic wave is, the higher the peak growth velocity of the dendrite tip. In addition, the time required for the peak growth velocity of the dendrite tips significantly decreased after the addition of ultrasound. This is because ultrasonic waves induce forced convection in the melt, driving the solute-enriched liquid from the upstream position to the downstream position. Consequently, a lower concentration region was formed in the upstream area, thus causing a faster growth velocity of the dendrite tip in the upstream liquid region.

3.2 Simulation of multiple equiaxed dendrite growth

In the simulations of multiple equiaxed dendrite growth, in addition to the position of the nuclei, the simulation conditions were consistent with those of the single equiaxed dendrite growth simulation. Figures 4(a)–4(d) show the morphological evolution of the equiaxed dendrites without ultrasound when the solid fraction was f_s = 5%, 25%, 50%, and 95%, respectively. Figures 4(e) and 4(f) show the final dendritic morphologies at a solid fraction of f_s = 95% when the ultrasonic amplitudes were A = 0.05 and 0.1 mm, respectively. Ultrasound had a strong influence on the

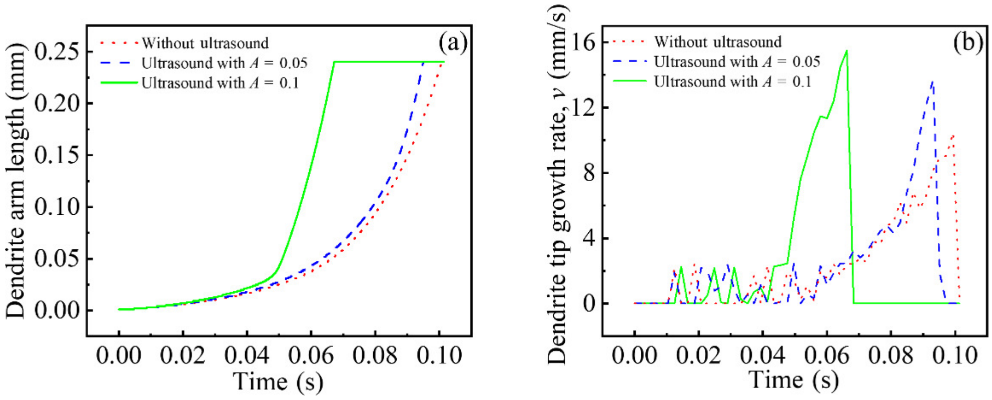

Fig. 3 Time evolution of (a) dendrite arm length and (b) growth rate of dendrite tip of a single equiaxed dendrite on upstream side in cases without ultrasound and with ultrasonic waves having amplitudes of 0.05 and 0.1 mm, respectively.

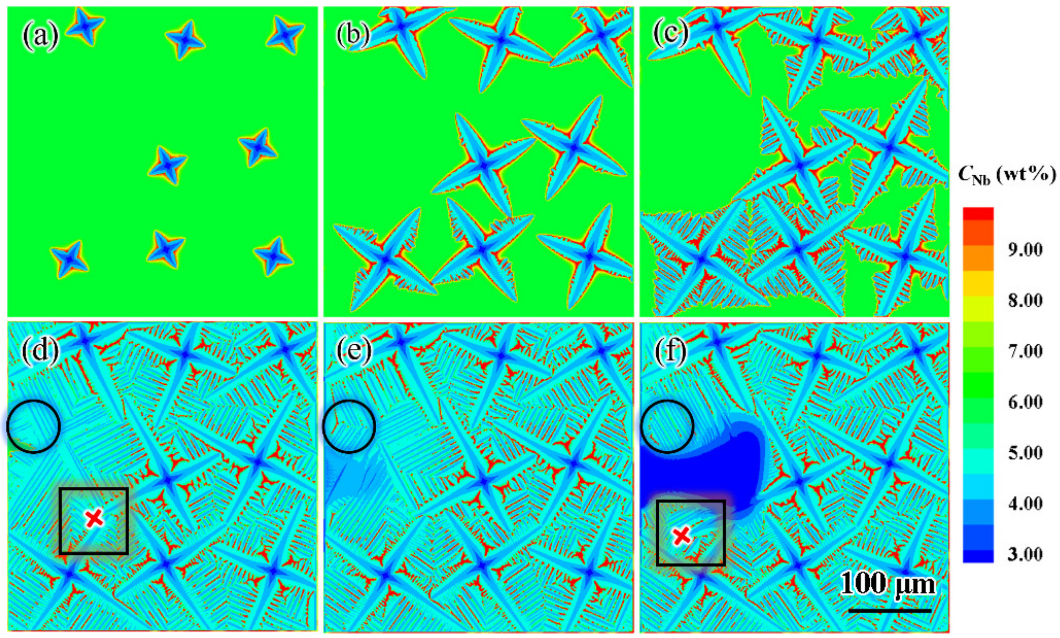

Fig. 4 Simulated morphological evolution of multiple equiaxed dendrites shown by concentration of solute Nb without ultrasound at f_s of (a) 5%, (b) 25%, (c) 50%, and (d) 95%, and with ultrasound having amplitudes of (e) 0.05 mm and (f) 0.1 at f_s = 95%.

growth of the equiaxed dendrites and their morphologies. As indicated by the squares in Figs. 4(d) and 4(f), ultrasound obviously promoted the growth of primary dendrites. Owing to the application of ultrasound, the growth rate of the upstream tip of the equiaxed dendrite closest to the ultrasound is significantly greater than that in the absence of ultrasound, as indicated by the red cross symbols. Owing to the competitive growth mechanism, it also hinders the growth of the dendrite arms that belong to the adjacent equiaxed dendrites. As indicated by the circles in Figs. 4(d)–4(f), on the other hand, the secondary dendrite arms were obviously thinner, and the secondary dendrite arm spacing was reduced under the effects of ultrasonic waves. In addition, due to the disturbance caused by ultrasonic waves, the concentration of solute Nb near the ultrasound source was significantly lower than that in other regions, and it became even lower as the ultrasonic amplitude increased. The low liquid concentration elevated the degree of solute undercooling and thus increased the growth rates of the dendrites in this region.

Quantitative analyses of the growth of multiple equiaxed dendrites under different ultrasonic conditions were conducted. Figure 5(a) shows that the evolution of the solid fraction varies with time. When there was no ultrasonic wave, the time required for the liquid phase to completely solidify was 0.114 s. When the ultrasonic amplitudes were A = 0.05 and 0.1 mm, however, the times were slightly reduced. Figure 5(b) shows the time evolution of the average solute concentration in the liquid phase as multiple equiaxed dendrites grew. During the solidification process, the average solute concentration in the liquid increased drastically. In the late stage of solidification, the liquid concentration slightly decreased. Moreover, for the cases with ultrasound, the average liquid concentrations were higher than those without ultrasound. Figures 3 and 5 show that the effect of ultrasound on single equiaxed dendrites is more obvious than that on multiple equiaxed dendrites. This is mainly attributed to the different effects of flow propagation in the liquid region for the cases of single and multiple equiaxed dendrites. In the later stages of multiple equiaxed dendrite growth, the high number of dendrites reduces the available space for full fluid motion, and the growth of neighboring dendrites also impacts the growth of the equiaxed dendrites. Therefore, the number of convections induced by ultrasound is effectively reduced. For a single equiaxed dendrite, however, there is still enough space at the end of solidification for flow propagation so that the patterns of the dendrites are significantly affected by ultrasonic flow.

3.3 Simulation of columnar dendrite growth

When simulating the growth of columnar dendrites, the cooling rate and temperature gradient were set to CR = 750 K/s and G = 150,000 K/m, respectively. The simulations were carried out without ultrasound and with ultrasound having amplitudes of A = 0.05 and 0.1 mm, respectively. Figures 6(a)–6(d) display the morphological evolution of the columnar dendrites when there was no ultrasonic wave at solid fractions of f_s = 10%, 30%, 60%, and 97%, respectively. Figures 6(e)–6(h) and 6(i)–6(l) display the columnar dendrite morphologies when the ultrasonic amplitudes were A = 0.05 and 0.1 mm, respectively. The ultrasonic wave promoted the growth of columnar dendrites that were nearest to the ultrasonic source but inhibited the growth of other columnar dendrites. In our study, the ultrasonic source was located at the left boundary of the melt. The ultrasonic source generated an acoustic stream and pressures in the melt, driving the movement of liquid atoms. These effects led to the redistribution of solutes within the melt. The strong acoustic effects induced drastic convection, which drove the solutes to be transported away from the region near the ultrasonic source, resulting in the formation of a low-concentration zone. In addition, the expelled solute atoms tend to form periodic high-concentration regions in the computational domain. The formation of alternative concentration distributions caused by ultrasonication will be investigated in our future work. It can be seen from the velocity vectors in Fig. 6(k) that the ultrasound causes forced convection toward the inside liquid region in the domain. Affected by these convections, the solute atoms rejected by the growing dendrite tips are driven in the direction away from the ultrasonic sound source, resulting in an uneven solute distribution. According to Eq. (3), as the actual liquid concentration near the ultrasonic source decreases, the solid fraction increases, which promotes the growth of the dendrites. The simulated larger dendrite arms are consistent with the experimental findings of Bruno Lebon *et al.* [35]. Moreover, this phenomenon became more obvious as the amplitude of the ultrasonic wave increased. Owing to the difference in the growth rate of columnar dendrites under the effects of ultrasonic waves, the competitive growth mode of columnar dendrites was modified. Thus, the primary dendrite spacing changed with increasing ultrasonic amplitude.

To study the effect of the ultrasonic amplitude on the primary dendrite arm spacing (PDAS), the cooling rate CR = 500 K/s and the temperature gradient G = 100,000 K/m were set unchanged, and the PDAS values were quantified. For the cases of no ultrasonic wave, the ultrasonic amplitude A = 0.05 and 0.1 mm. As shown in Fig. 7, with the addition of ultrasonic waves and increasing ultrasonic amplitude from 0.05 to 0.1 mm, the primary dendrite spacing first decreased but then increased. The addition

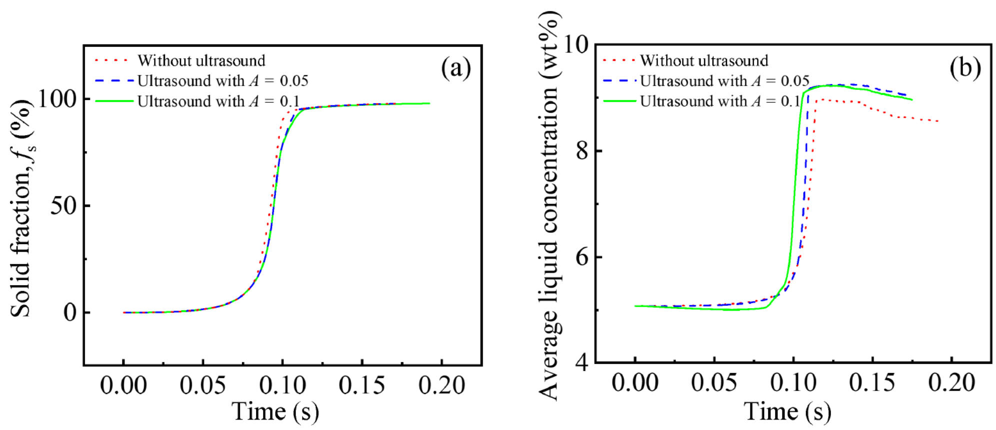

Fig. 5 Simulated evolution of (a) solid fraction and (b) average liquid concentration in processes of multiple equiaxed dendrite growth. Dotted, dashed, and solid lines represent cases without ultrasound and with ultrasound having amplitudes of 0.05 and 0.1 mm, respectively.

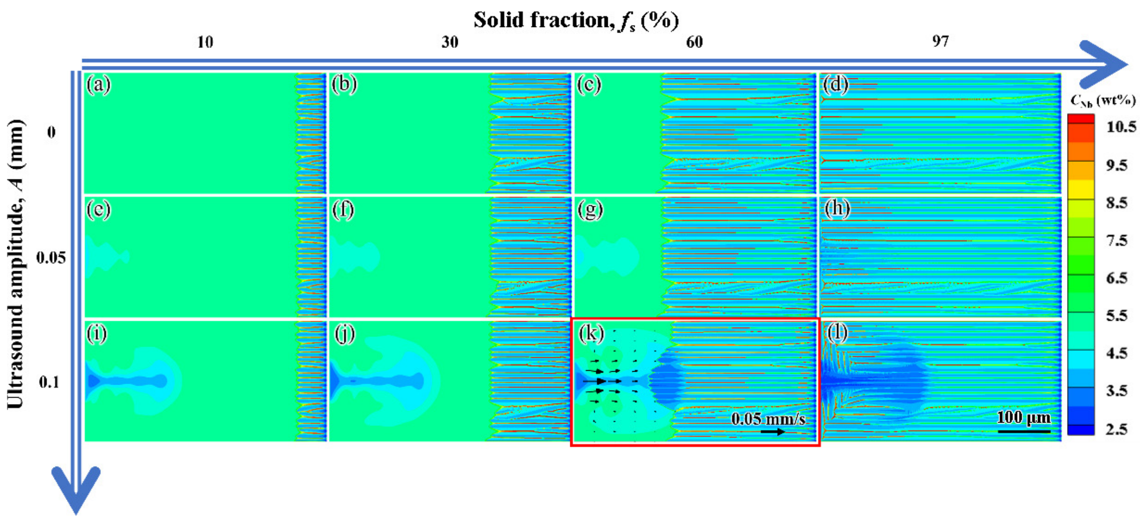

Fig. 6 Simulated morphological evolution of columnar dendrites under conditions (a–d) without ultrasound, with ultrasound having amplitudes of (e–h) A = 0.05 mm and (i–l) A = 0.1 mm, respectively. Solid fractions of insets are (a, e, i) f_s = 10%, (b, f, j) f_s = 30%, (c, g, k) f_s = 60%, and (d, h, l) f_s = 97%, respectively. Black arrows in (k) represent velocity vectors in liquid caused by ultrasound.

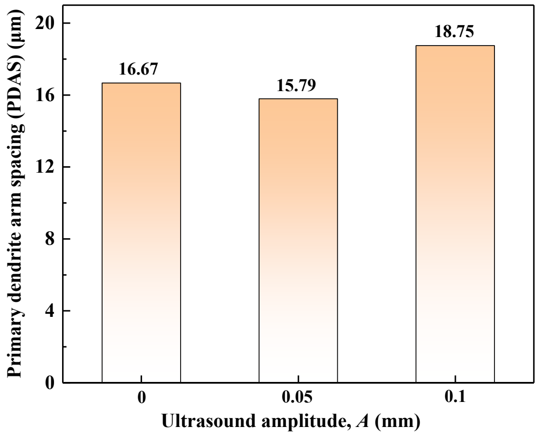

Fig. 7 Simulated primary dendrite arm spacing varying with ultrasonic amplitudes at CR = 750 K/s and G = 150,000 K/m.

of ultrasound increased the degree of undercooling at the solidification front, thereby promoting the growth of columnar dendrites and refining dendrites. However, as the amplitude increased further, the columnar dendrites close to the ultrasonic sound source grew too fast, leading to the merging of the dendrite arms and a reduction in the number of columnar dendrites, resulting in the formation of coarse columnar dendrites.

4 Conclusions

To explore the influence of ultrasonication on the solidification microstructure of an IN718 alloy, a coupled CA–LB model was developed to simulate dendrite growth under forced convection induced by ultrasonic waves. The simulation of the transient flow velocity distribution in the melt caused by ultrasonic propagation was performed via this model. The good agreement between the simulation results and the analytical model demonstrates the quantitative capability of the model used in the present work.

For the growth of a single equiaxed dendrite, owing to the influence of ultrasonic waves on the concentration field, the growth rate of the dendrite arm near the ultrasonic field was faster than that of the others. The secondary dendrite arms were more likely to grow toward the ultrasonic sound source, and the secondary dendrite arms were more developed. The simulations of multiple equiaxed dendrites revealed that the presence of ultrasonic waves drastically influenced the dendrite morphology, but its impact on the complete solidification time was not significant. In the cases with ultrasonication, the average solute concentration in the liquid phase was relatively low in the initial stage of solidification, while the average solute concentration in the liquid phase was relatively high in the final stage of solidification. The simulation results of the growth of columnar dendrites show that ultrasonic waves promoted the growth of the columnar dendrites that were nearest to the ultrasound source. Therefore, the competitive growth mode of columnar dendrites was affected by ultrasonic waves, which influenced the primary dendrite arm spacing.

Acknowledgements

This research was funded by the National Natural Science Foundation of China (No. 52475389).

Availability of data and materials

Not applicable.

Competing interests

The authors have no competing interests to declare that are relevant to the content of this article.

References

[1] Cadiou S, Courtois M, Carin M, *et al.* Heat transfer, fluid flow and electromagnetic model of droplets generation and melt pool behaviour for wire arc additive manufacturing. *Int J Heat Mass Tran* 2020, **148**: 119102.
[2] Wu BT, Pan ZX, Ding DH, *et al.* A review of the wire arc additive manufacturing of metals: Properties, defects and quality improvement. *J Manuf Process* 2018, **35**: 127–139.
[3] Wang H, Liu K, Wu H, Zhou JB, Li, J, Zhang QL. Research status and prospect of additive manufacturing technology of ship aluminum alloys. *Dev Appl Mater* 2024, **39**: 17–27. (in Chinese)
[4] Yuan L, Lee PD. Dendritic solidification under natural and forced convection in binary alloys: 2D versus 3D simulation. *Model Simul Mater Sc* 2010, **18**: 055008.
[5] Van D, Dinda GP, Park J, *et al.* Enhancing hardness of Inconel 718 deposits using the aging effects of cold metal transfer-based additive manufacturing. *Mater Sci Eng A* 2020, **776**: 139005.
[6] Hosseini E, Popovich VA. A review of mechanical properties of additively manufactured Inconel 718. *Addit Manuf* 2019, **30**: 100877.
[7] Francois MM, Sun A, King WE, *et al.* Modeling of additive manufacturing processes for metals: Challenges and opportunities. *Curr Opin Solid St M* 2017, **21**: 198–206.
[8] Ma J, Wang B, Zhao SL, *et al.* Incorporating an extended dendritic growth model into the CAFE model for rapidly solidified non-dilute alloys. *J Alloys Compd* 2016, **668**: 46–55.
[9] Zhu MF, Tang QY, Zhang QY, *et al.* Cellular automaton modeling of microstructure evolution during alloy solidification. *Acta Metall Sin* 2016, **52**: 1297–1310. (in Chinese)
[10] Kundin J, Mushongera L, Emmerich H. Phase-field modeling of microstructure formation during rapid solidification in Inconel 718 superalloy. *Acta Mater* 2015, **95**: 343–356.
[11] Koepf JA, Gotterbarm MR, Markl M, *et al.* 3D multi-layer grain structure simulation of powder bed fusion additive manufacturing. *Acta Mater* 2018, **152**: 119–126.
[12] Xiao WJ, Li SM, Wang CS, *et al.* Multi-scale simulation of dendrite growth for direct energy deposition of nickel-based superalloys. *Mater Design* 2019, **164**: 107553.
[13] Qiu TS, Zhu DM, Wu CY, *et al.* Lattice Boltzmann model for simulation on leaching process of weathered elution-deposited rare earth ore. *J Rare Earth* 2017, **35**: 1014–1021.
[14] Sun DK, Zhu MF, Pan SY, *et al.* Lattice Boltzmann modeling of dendritic growth in a forced melt convection. *Acta Mater* 2009, **57**: 1755–1767.
[15] Zhang A, Du JL, Guo ZP, *et al.* A phase-field lattice-Boltzmann study on dendritic growth of Al–Cu alloy under convection. *Metall Mater Trans B* 2018, **49**: 3603–3615.
[16] Zhao YF, Koizumi Y, Aoyagi K, *et al.* Molten pool behavior and effect of fluid flow on solidification conditions in selective electron beam melting (SEBM) of a biomedical Co–Cr–Mo alloy. *Addit Manuf* 2019, **26**: 202–214.
[17] Zakirov A, Belousov S, Bogdanova M, *et al.* Predictive modeling of laser and electron beam powder bed fusion additive manufacturing of metals at the mesoscale. *Addit Manuf* 2020, **35**: 101236.
[18] Sun DK, Pan SY, Han QY, *et al.* Numerical simulation of dendritic growth in directional solidification of binary alloys using a lattice Boltzmann scheme. *Int J Heat Mass Tran* 2016, **103**: 821–831.
[19] Liu DH, Wang Y. Mesoscale multi-physics simulation of rapid solidification of Ti–6Al–4V alloy. *Addit Manuf* 2019, **25**: 551–562.
[20] Zhang YB, Lu YP, Jie JC, *et al.* Overflowing phenomenon during ultrasonic treatment in Al–Si alloys. *T Nonferr Metal Soc* 2013, **23**: 3242–3248.
[21] Han YF, Li K, Wang J, *et al.* Influence of high-intensity ultrasound on grain refining performance of Al–5Ti–1B master alloy on aluminium. *Mat Sci Eng A* 2005, **405**: 306–312.

[22] Jian X, Meek TT, Han Q. Refinement of eutectic silicon phase of aluminum A356 alloy using high-intensity ultrasonic vibration. *Scripta Mater* 2006, **54**: 893–896.
[23] Li XT, Li TJ, Li XM, *et al*. Study of ultrasonic melt treatment on the quality of horizontal continuously cast Al–1%Si alloy. *Ultrason Sonochem* 2006, **13**: 121–125.
[24] Zhang SL, Zhao YT, Cheng XN, *et al*. High-energy ultrasonic field effects on the microstructure and mechanical behaviors of A356 alloy. *J Alloys Compd* 2009, **470**: 168–172.
[25] Haghayeghi R, Kapranos P. Solidification of Pb–Sn alloys under ultrasonic field. *Mater Lett* 2014, **126**: 244–248.
[26] Jia S, Nastac L. The influence of ultrasonic stirring on the solidification microstructure and mechanical properties of A356 alloy. *Chem Mater Eng* 2013, **1**: 69–73.
[27] Hu YJ, Wang JY, Zhai W, *et al*. Ultrasounds induced microstructure transition and improved mechanical property of directionally solidified ternary Cu–Al–Ni alloy. *Metall Mater Trans B* 2024, **55**: 3736–3749.
[28] Li AQ, Jiang RP, Hai XQ, *et al*. Numerical simulation of physical field during different ultrasonic-power-assisted casting of 7085 aluminum alloy. *Adv Eng Mater* 2024, **26**: 2400458.
[29] Chen BY, Zhang QY, Sun DK, *et al*. Effects of shear flows on columnar dendritic microstructure during rapid solidification of IN718 alloy: A cellular automaton-lattice Boltzmann modeling study. *J Cryst Growth* 2022, **585**: 126583.
[30] Nastac L. Numerical modeling of solidification morphologies and segregation patterns in cast dendritic alloys. *Acta Mater* 1999, **47**: 4253–4262.
[31] Zhu MF, Stefanescu DM. Virtual front tracking model for the quantitative modeling of dendritic growth in solidification of alloys. *Acta Mater* 2007, **55**: 1741–1755.
[32] Hunziker O, Dye D, Reed RC. On the formation of a centreline grain boundary during fusion welding. *Acta Mater* 2000, **48**: 4191–4201.
[33] Kurz W, Giovanola B, Trivedi R. Theory of microstructural development during rapid solidification. *Acta Metall* 1986, **34**: 823–830.
[34] Walton O, Haghayeghi R, Lazaro BS, DMS, Dai Q, Tan Y. Simulation of acoustic wave attenuation using lattice Boltzmann method. *Journal of Xi'an Jiaotong University* 2007, **1**: 5–8. (in Chinese)
[35] Bruno Lebon GS, Salloum-Abou-Jaoude G, Eskin D, *et al*. Numerical modelling of acoustic streaming during the ultrasonic melt treatment of direct-chill (DC) casting. *Ultrason Sonochem* 2019, **54**: 171–182.